Chapter 14
Magnetic Field Amplification in Hypermassive Neutron Stars via the Magnetorotational Instability

Daniel M. Siegel and Riccardo Ciolfi

Abstract Mergers of binary neutron stars likely lead to the formation of a hypermassive neutron star (HMNS), which is metastable and eventually collapses to a black hole. This merger scenario is thought to explain the phenomenology of short gamma-ray bursts (SGRBs). The very high energies observed in SGRBs have been suggested to stem from neutrino-antineutrino annihilation and/or from very strong magnetic fields created during or after the merger by mechanisms like the magnetorotational instability. Here, we report on results that show for the first time the development of the magnetorotational instability in HMNSs in three-dimensional, fully general-relativistic magnetohydrodynamic simulations. This instability amplifies magnetic fields exponentially and could be a vital ingredient in solving the SGRB puzzle.

14.1 Introduction

A significant fraction of neutron star–neutron star (NS–NS) binary mergers can lead to the formation of a hypermassive neutron star (HMNS) that eventually collapses to a stellar-mass black hole, surrounded by a hot and dense accretion torus (e.g. [1, 2]). Besides being among the most promising sources for the first direct detection of gravitational waves with advanced ground based interferometers such as Advanced LIGO and Virgo [3, 4], the inspiral and coalescence of NS–NS binaries is also thought to be the progenitor system for short gamma-ray bursts (SGRBs), the most luminous explosions observed in the universe (see, e.g., [5, 6] for a review). The association of SGRBs with NS–NS coalescence is supported on both observational [7, 8] and theoretical [9, 10] grounds. The observed SGRB fluxes, their cosmological distances and their duration of <2 s require highly relativistic motion with Lorentz factors of up to

D.M. Siegel (✉) · R. Ciolfi
Max-Planck-Institut für Gravitationsphysik (Albert-Einstein-Institut),
Am Mühlenberg 1, 14476 Potsdam, Germany
e-mail: daniel.siegel@aei.mpg.de

R. Ciolfi
e-mail: riccardo.ciolfi@aei.mpg.de

P. Nicolini et al. (eds.), *1st Karl Schwarzschild Meeting on Gravitational Physics*,
Springer Proceedings in Physics 170, DOI 10.1007/978-3-319-20046-0_14

several hundreds to resolve the so-called compactness problem [5], which states that in the absence of high Lorentz factors, SGRBs would show a thermal spectrum—in contradiction to the observed non-thermal spectra. Apart from neutrino-antineutrino annihilation as one possibility, the enormous amounts of energy needed to generate such extreme velocities have been suggested to stem from strong magnetic fields produced during/after the merger process by mechanisms such as the Kelvin-Helmholtz (KH) [11–13] and the magnetorotational instability (MRI) [14, 15], or by high field strengths generated in the torus after the central black hole has formed (as in [9]). One advantage of the former mechanisms is that they do not depend on the creation and properties of a torus and that they would already act prior to the collapse. While the amount of amplification through the KH instability, triggered when the two stars enter into contact, is controversial and maybe limited to only one order of magnitude [11, 13], the MRI triggered in the metastable differentially rotating HMNS appears to constitute a promising amplification mechanism, especially in the light of recent results indicating a rather stiff equation of state [16, 17]. The latter results suggest that HMNSs are indeed a likely outcome of NS–NS mergers [18, 19], and that they are probably longer lived than previously thought, providing more time for a potential MRI to act. However, simulating the MRI in three dimensions under the extreme physical conditions of HMNS interiors is a challenge and had not been accomplished until very recently [20].

Here, we elaborate on these recent results that have shown for the first time direct evidence for the MRI in the interior of a HMNS in global, three-dimensional and fully general-relativistic magnetohydrodynamic simulations.

14.2 Capturing the MRI in HMNSs

The magnetorotational instability [21, 22] can be triggered in differentially rotating magnetized fluids [23] and refers to modes that grow exponentially from initial seed perturbations. From a linear perturbation analysis of the Newtonian MHD equations, one can estimate the characteristic timescale $\tau_{\rm MRI}$ and wavelength $\lambda_{\rm MRI}$ for the fastest-growing mode with wavevector $\mathbf{k}$ by

$$\tau_{\rm MRI} \sim \Omega^{-1}\,, \qquad \lambda_{\rm MRI} \sim \left(\frac{2\pi}{\Omega}\right)\left(\frac{\mathbf{B}\cdot\mathbf{e_k}}{\sqrt{4\pi\rho}}\right)\,, \tag{14.1}$$

where Ω denotes the angular velocity of the fluid, ρ the density, $\mathbf{B}$ the magnetic field, and $\mathbf{e_k}$ the unit vector in direction of $\mathbf{k}$ [23, 24]. We note that there is no general analytic description of the MRI within general-relativistic MHD to date. Nevertheless, we can compare our fully general-relativistic numerical results with the above analytical estimates, provided that the Newtonian predictions are translated into general relativity by employing equivalence principle arguments [20].

Resolving the MRI in an MHD simulation is a challenge, as $\lambda_{\rm MRI}$ is typically much smaller than the characteristic length scale of the astrophysical system under

study. Local simulations of only a small part of the system (e.g. [25]) or simulations in axisymmetry [14, 15] are usually conducted in order to render the problem computationally affordable. In the case of HMNSs, capturing the MRI for realistic (i.e. relatively low) magnetic field strengths is particularly demanding due to the extremely high densities and high angular velocities involved (cf. (14.1)).

Here, we discuss global three-dimensional simulations, which start from a typical axisymmetric and differentially rotating HMNS model of mass $M = 2.23\,\mathrm{M}_\odot$ and central angular velocity $\Omega_c = 2\pi \times 7\,\mathrm{kHz}$ (representing the outcome of a NS–NS merger) and employ a four-level nested-boxes grid hierarchy, with the finest refinement level covering the HMNS at all times. In order to capture the MRI and despite the very high resolutions used here (with finest grid spacing of $h = 44\,\mathrm{m}$), high initial magnetic field strengths of $B^{\mathrm{in}} = (1{-}5) \times 10^{17}\,\mathrm{G}$ have to be employed, assuming that these field strengths have previously been generated by compression during the merger, the KH instability, magnetic winding and previous MRI activity. However, it is important to point out that these field strengths are still very small in terms of the average magnetic-to-fluid pressure ratio, which is between $(0.045 - 1.2) \times 10^{-2}$. In order to reduce the computational costs, a reflection symmetry across the $z = 0$ plane and a $\pi/2$ rotation symmetry around the z-axis have been applied. By performing two additional simulations, removing either the reflection symmetry or replacing the rotation symmetry by a π symmetry, we have verified that these discrete symmetries do not significantly influence our results. For instance, the relative differences for the maximum of the toroidal field strength (as plotted in Fig. 14.3) are well below 10^{-3} up to $t \approx 0.4\,\mathrm{ms}$ when the star starts collapsing to a black hole.

14.3 Discussion of Simulation Results

Figure 14.1 provides a representative overview of the HMNS evolution: the initial axisymmetric configuration, which shows a highly flattened HMNS due to rapid rota-

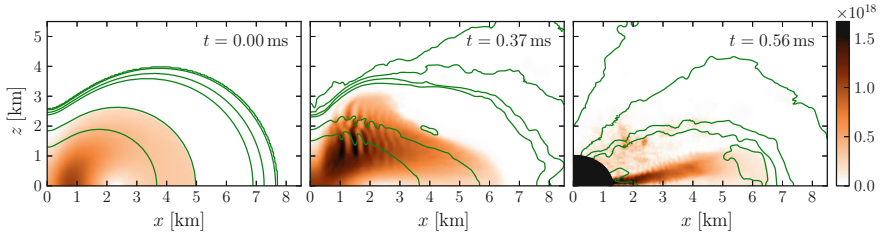

Fig. 14.1 Three characteristic stages of the HMNS evolution represented by a cut in the x–z plane, showing the colour-coded norm of the magnetic field (in G) and selected density contours: initial HMNS model, pronounced MRI development, and early post-collapse phase with a black hole (horizon is masked) surrounded by a magnetized torus

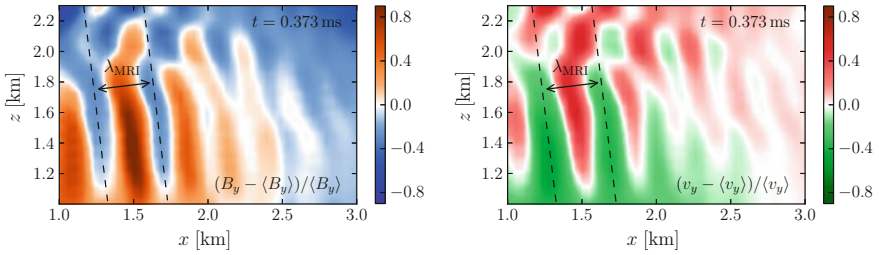

Fig. 14.2 Channel flow structures as seen in the toroidal magnetic field (*left*) and the toroidal component of the 3-velocity field (*right*). Shown are the relative deviations from the mean value in the region considered here. The wavelength of the fastest-growing MRI mode can be clearly identified

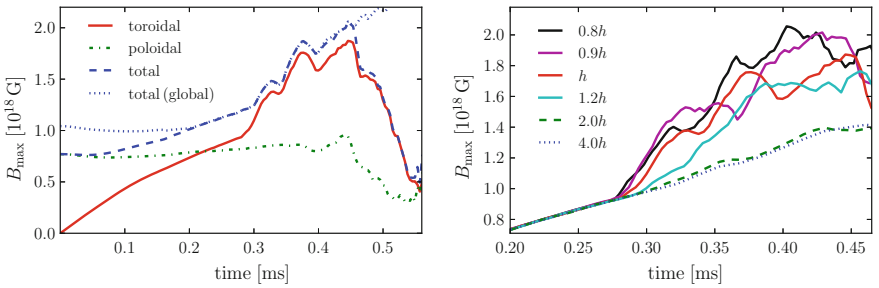

Fig. 14.3 *Left* Maximum magnetic field strength for the toroidal, poloidal and total magnetic field in the region $(x, z) = [1.0, 3.0] \times [1.0, 2.3]$ km, and the corresponding total evaluated in the entire x–z plane. *Right* Maximum toroidal magnetic field strengths in the same region for runs with different resolution (but otherwise identical), with finest grid spacings between $(4-0.8)$ h, where $h = 44$ m refers to the fiducial value

tion; the stage of a developed MRI, indicated by the ripples in the magnetic field and density; the early post-collapse phase showing a black hole surrounded by a magnetized and geometrically thick torus. The "ripple patterns" seen in this simulation are similar to the coherent channel flow structures (WKB-like modes) observed in local axisymmetric Newtonian MRI simulations, which are the characteristic signatures of this instability (e.g. [25]). This is the first time in global general-relativistic simulations of HMNSs that such rapidly-growing and spatially-periodic structures are observed. Figure 14.2 displays the channel flow structures in a zoomed-in version for the toroidal magnetic field and the toroidal component of the velocity field. The onset of channel-flow merging (reminiscent of the results reported in [25]) is evident in the upper part of the panels.

The left panel of Fig. 14.3 shows the maximum field strength for the toroidal, poloidal and total magnetic field in the region $(x, z) \in [1.0, 3.0] \times [1.0, 2.3]$ km, where the instability develops most prominently, along with the analogous quantity for the total field evaluated over the entire x–z plane. The purely poloidal initial seed field geometry is lost very soon due to magnetic winding, which leads to a linear

increase in the toroidal field strength. At $t \approx 0.3$ ms, exponential magnetic field amplification due to the MRI sets in and lasts up to $t \approx 0.4$ ms when the star starts collapsing to a black hole. It is important to point out that even during this very short time frame, the MRI contributes significantly to a global magnetic field amplification of the system (compare local with global maximum of the total field).

The right panel of Fig. 14.3 demonstrates that the onset of the instability is well resolved. While any sign of the instability is absent in the case where there are less than five grid points per wavelength of the fastest-growing mode (as given by (14.1)), we gradually recover the growth rate of the fastest-growing mode with increasing resolution. The extracted values for this growth rate agree within error bars among the three highest-resolution runs, and the resulting value of $\tau_{\rm MRI} = (8.2 \pm 0.4) \times 10^{-2}$ ms is in order-of-magnitude agreement with the Newtonian analytic prediction from (14.1) for the considered region once translated to our general-relativistic setting, $\tau_{\rm MRI} = (4-5) \times 10^{-2}$ ms. Also the wavelength of the fastest-growing mode as measured with a Fourier analysis of the magnetic field in the selected region ($\lambda_{\rm MRI} \approx 0.4$ km) is in order-of-magnitude agreement with the corrected Newtonian analytic prediction from (14.1) for this region, $\lambda_{\rm MRI} \approx (0.5-1.5)$ km. For further details and verification of additional properties of the MRI as expected from local Newtonian simulations in other astrophysical systems, we refer to [20].

14.4 Conclusion

The simulations discussed here have shown for the first time direct evidence for the MRI in HMNSs in three-dimensional, fully general-relativistic MHD simulations. This evidence manifests itself, e.g., in the presence of coherent channel flow structures, which have not been previously observed in three-dimensional general-relativistic MHD simulations. The growth of these structures coincides with exponential growth in the toroidal field strength. Furthermore, the two characteristic quantities of the instability, the growth time and wavelength of the fastest-growing mode, were measured directly, and the resulting values are in order-of-magnitude agreement with the simplified Newtonian analytical estimates, once the latter have been corrected for coordinate effects due to the general relativistic framework of the simulations.

It is interesting to note that these simulations also represent the first detailed observation of the MRI in the strong gravity regime, where the characteristic length scale of spacetime curvature becomes comparable to the wavelength of the fastest-growing MRI mode. Despite the fact that the existence of WKB-type modes becomes less obvious in this context, these modes are observed and the idealized Newtonian analytic description still seems to provide reasonable predictions.

The global magnetic field amplification due to the MRI leads to very strong magnetic fields that at least for some time stay in the vicinity of the newly formed black hole, and can thus potentially contribute to power a relativistic jet launched by the black hole torus system. Therefore, the presence of the MRI in HMNSs is of great

astrophysical importance, as it could be a vital ingredient in solving the compactness problem of SGRBs.

One open question is to understand how much amplification can be achieved in a HMNS, before the dominant saturation mechanisms take place. In our model, the relatively short life of the HMNS limits the amplification to less than one order of magnitude. At the time of the collapse there is still no sign of saturation, which suggests the possibility of much higher magnetic field amplification in longer-lived models. This will be the focus of future studies.

Acknowledgments DMS greatly acknowledges the award of the first Karl Schwarzschild Prize sponsored by Springer for the best talk in the student section of the first Karl Schwarzschild Meeting, held in Frankfurt, Germany, July 2013. DMS also thanks the organizers of this meeting for travel support.

References

1. M. Shibata, K. Taniguchi, Phys. Rev. D **73**, 064027 (2006)
2. L. Rezzolla, L. Baiotti, B. Giacomazzo et al., Class. Quantum Grav. **27**(11), 114105 (2010)
3. G.M. Harry et al., Class. Quantum Grav. **27**, 084006 (2010)
4. T. Accadia, F. Acernese, F. Antonucci et al., Class. Quantum Grav. **28**(11), 114002 (2011)
5. T. Piran, Rev. Mod. Phys. **76**, 1143 (2004)
6. N. Gehrels, E. Ramirez-Ruiz, D.B. Fox, Ann. Rev. Astron. and Astrophys. **47**, 567 (2009)
7. S.D. Barthelmy, G. Chincarini, D.N. Burrows et al., Nature **438**, 994 (2005)
8. N. Gehrels, C.L. Sarazin, P.T. O'Brien et al., Nature **437**, 851 (2005)
9. L. Rezzolla, B. Giacomazzo, L. Baiotti et al., Astrophys. J. **732**(11), L6 (2011)
10. S. Rosswog, T. Piran, E. Nakar, Mon. Not. R. Astron. Soc. **430**, 2585 (2013)
11. R.H. Price, S. Rosswog, Science **312**, 719 (2006)
12. M. Anderson, E.W. Hirschmann, L. Lehner et al., Phys. Rev. Lett. **100**, 191101 (2008)
13. B. Giacomazzo, R. Perna, Astrophys. J. Lett. **771**, L26 (2013)
14. M.D. Duez, Y.T. Liu, S.L. Shapiro et al., Phys. Rev. D **73**, 104015 (2006)
15. M.D. Duez, Y.T. Liu, S.L. Shapiro et al., Phys. Rev. Lett. **96**(3), 031101 (2006)
16. P.B. Demorest, T. Pennucci, S.M. Ransom et al., Nature **467**, 1081 (2010)
17. J. Antoniadis, P.C.C. Freire, N. Wex et al., Science **340**, 448 (2013)
18. K. Hotokezaka, K. Kyutoku, H. Okawa et al., Phys. Rev. D **83**(12), 124008 (2011)
19. K. Hotokezaka, K. Kiuchi, K. Kyutoku et al., Phys. Rev. D **87**(2), 024001 (2013)
20. D.M. Siegel, R. Ciolfi, A.I. Harte et al., Phys. Rev. D **87**(12), 121302(R) (2013)
21. E.P. Velikhov, Sov. Phys. JETP **36**, 995 (1959)
22. S. Chandrasekhar, Proc. Natl. Acad. Sci. **46**, 253 (1960)
23. S.A. Balbus, J.F. Hawley, Astrophys. J. **376**, 214 (1991)
24. S.A. Balbus, Astrophys. J. **453**, 380 (1995)
25. M. Obergaulinger, P. Cerdá-Durán, E. Müller et al., Astron. Astrophys. **498**, 241 (2009)